Electrophysical response of Langmuir-Blodgett thin films from carbon nanotubes decorated by organometallic compound to ionizing low-energy gamma irradiation

H. V. Krylova

Belarusian State University, Minsk, BELARUS

Collaboration:

E. A. Awdanina, BSU, Minsk, Belarus
I. V. Lipnevich, BSU, Minsk, Belarus
A. I. Timoshchenko, BSU, Minsk, Belarus

OUTLINE

I. Introduction

I.1. Radiation resistivity of graphene and carbon nanotubes (CNT): radiation point defects

CNT is a rolled-up graphene flake (see Fig.)

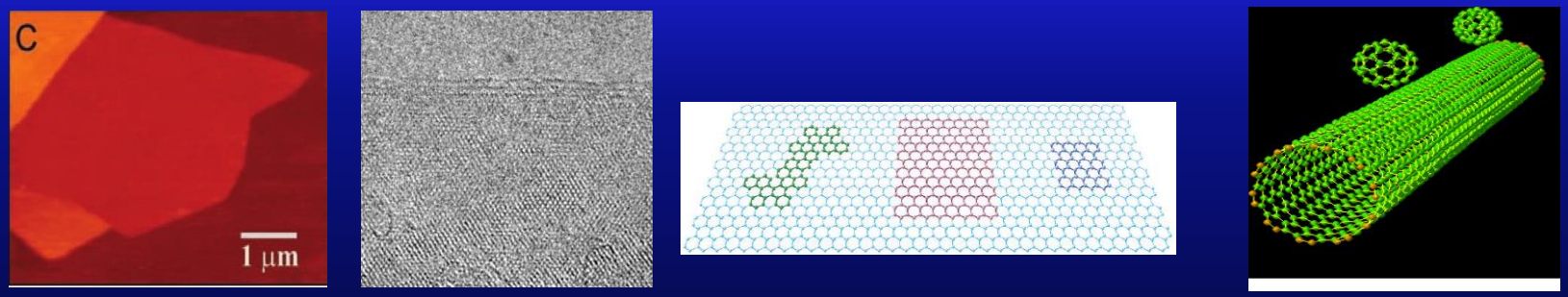

Figure : (left) An AFM image of single- and multi-layer graphene on a SiO_2/Si substrate [K.S. Novoselov, A.K. Geim (2004)]. (middle) Atomic scale TEM image of suspended graphene. Few- to single-layer graphene sheet showing long range crystalline order, scale bar 1 nm

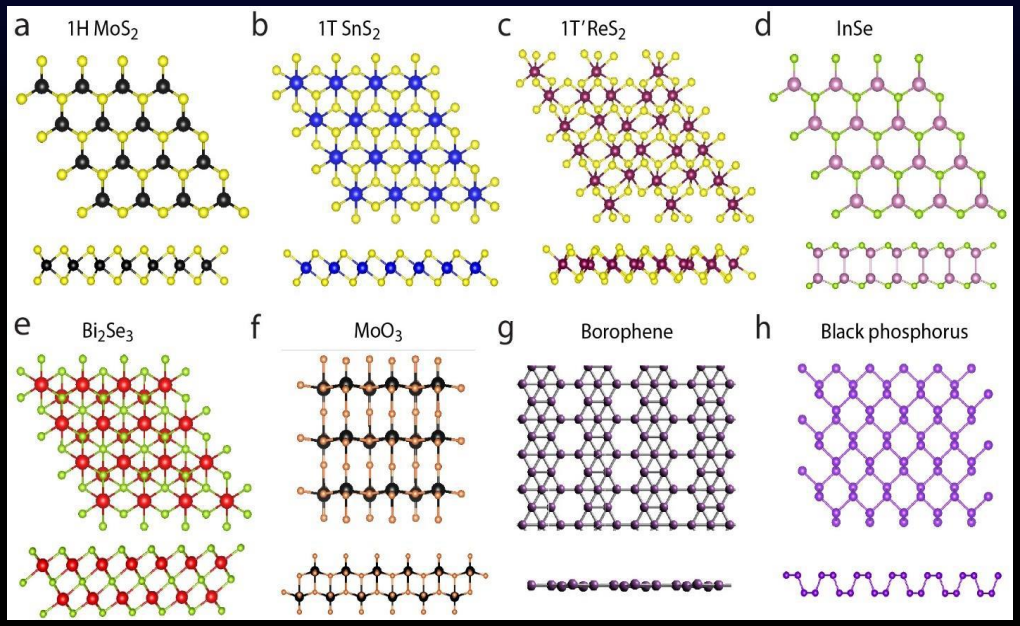

Figure: **Crystal structure of graphene-like materials (top and side views).** [V.K. Sangwan, M.C. Hersam (2018)]

I. Introduction : continued

I.1. Radiation resistivity of graphene and carbon nanotubes (CNT): continued

Thickness of graphene is equal to size of single atom. Although the graphene thickness is very small, radiation resistivity is a feature of graphene and carbon nanotube [Hai Huang et al. (2016)]. Assuming point defects in a form of interstitials and vacancies simulations yield this feature.

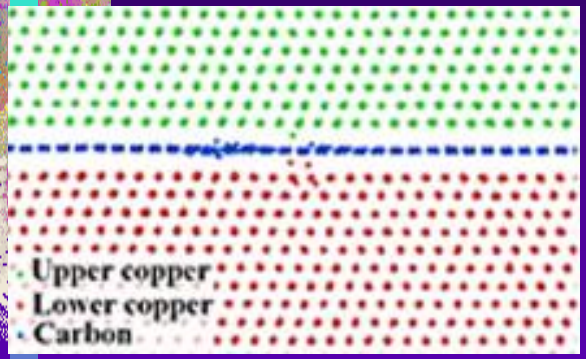

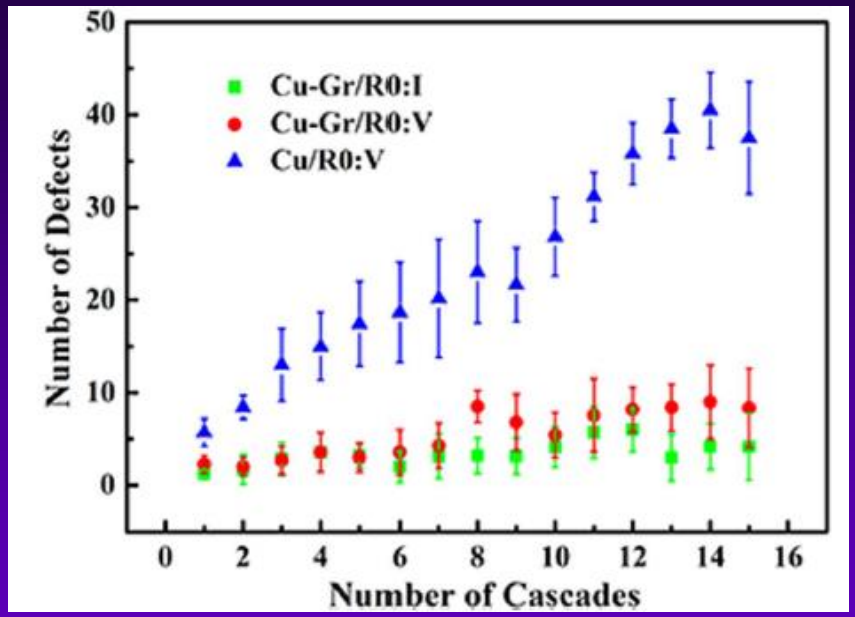

Figure : (left) Cu–Graphene – nanocomposite under irradiation,
(right) The number of surviving point defects being interstitials (I) and vacancies (V) in the bulk region of Cu–Graphene – nanocomposite versus the number of collision cascades. The green box and red circle represent the numbers of interstitials and vacancies in the bulk region, respectively.

I. Introduction : continued

I.1. Radiation resistivity of graphene and carbon nanotubes (CNT): continued

Molecular dynamics methods to simulate radiation damage of graphene through point defects (interstitials and vacancies) have demonstrated that graphene monolayer located between two thick Cu-layers prevents penetration of radiation defects and respectively, radiation in bulk(see fig.). The carbon atoms, which are knocked out of the graphene plane due to cascades, cannot escape from the graphene to enter the deep bulk region. On the contrary, they are absorbed on the surface of graphene as you can see in fig.

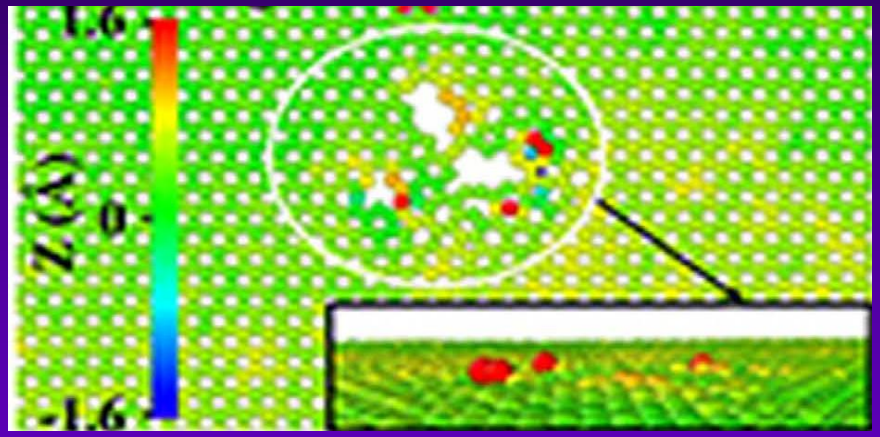

Figure : The graphene of Cu–Graphene composite obtained after a collision cascade. Carbon atoms are colored according to their z-coordinates centering on graphene layer. The damage region of graphene is singled out with a white oval and enlarged in the insets.

I. Introduction : continued

I.2. Rainbow channelling effect: surface radiation defects : continued

The broadband channeling of positively charged particles in thin crystals and carbon nanotubes is named a rainbow channelling effect. The rainbow channelling effect is observed in the transverse plane of carbon nanotube. The broadband channeling testifies that protons and positrons suffer deflections on surface states of nanotube walls as light on water drops. It has been shown both theoretically and experimentally that the rainbow effect dominantly determines the angular distributions of the positively charged particles channeled in thin crystals and carbon nanotubes. In [S. Petrovic et al. (2013), M. Cosic et al. (2014, 2016)] utilizing Thomas-Fermi interaction potential of a positron and a nanotube atom demonstrated that collisions with electrons can be neglected.

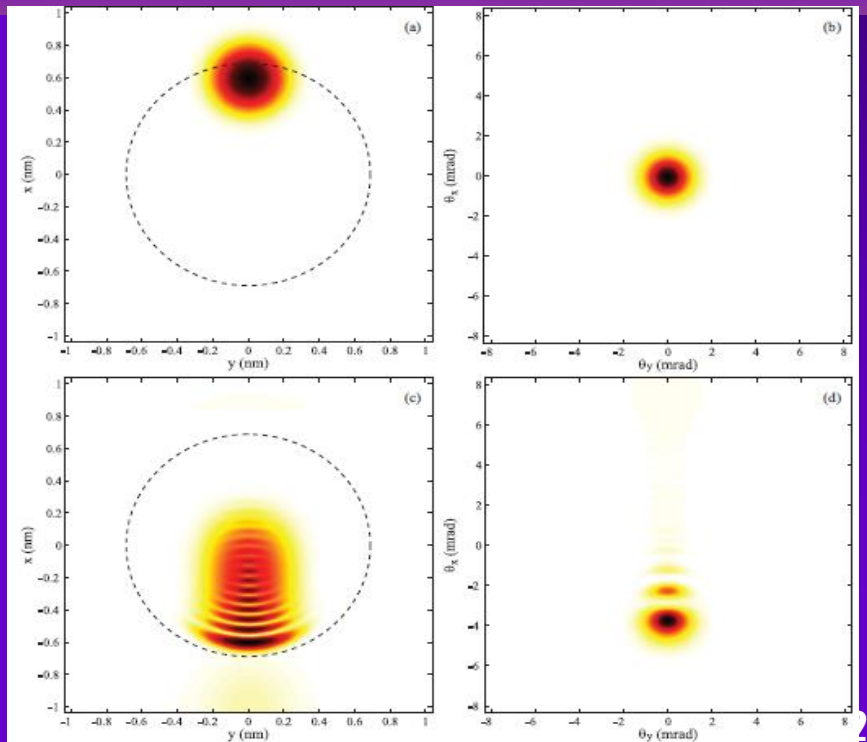

Figure : (a) Two-dimensional initial spatial distribution of a 1-MeV positron represented as the Gaussian wave packet with $\sigma_\theta = 0.1\theta_c$ and (x_0,y_0) = (0.599 nm, 0), (b) the corresponding initial angular distribution, (c) the resulting spatial distribution of the positron transmitted through a 200-nm-long (11,9) SWCN, and (d) the corresponding resulting angular distribution. The dashed circle, appearing in panels (a) and (c), represents the nanotube wall.

I. Introduction : continued

I.2. Rainbow channelling effect: surface radiation defects : continued

So, radiation defects for CNT are bound to CNT-surface as you can see in fig. According to experimental data and theoretical studies, there is a mechanism to fasten knocked-out atoms on CNT-surface. This mechanism is a cause that a production of charge carriers and defects in graphene-like materials are dropped at growing energy of the projectiles [Novikov (2010)]. In contrast to it, a number of produced charge carriers and defects in bulk materials increases with growing energy of the projectiles.

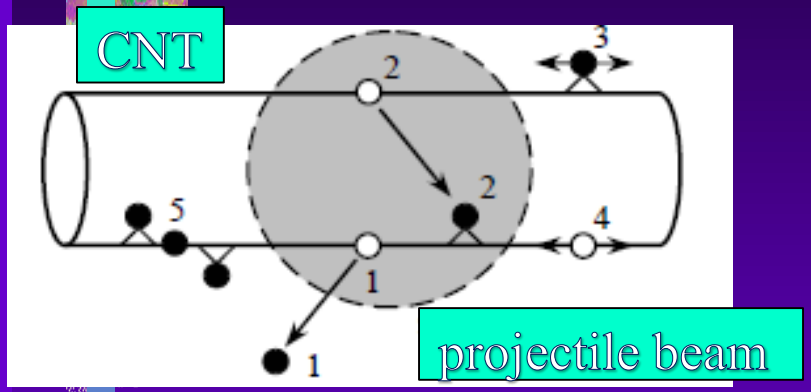

Figure : Sketch of radiation defects: 1 – vacancy, 2 – creation of vacancy with absorption of knocked-on atom at nanotube wall, 3 – migration of absorbed atom, 4 – migration of vacancy, 5 – movement of absorbed atom through nanotube wall.

This conjecture clarifies the recovering ability of graphene-like materials including CNTs. However, origin of this confinement of atom C is unknown. Graphene and another Dirac materials can host Majorana bound defect states.

In this work I would like to show the topologically prevented Majorana states and chiral charge-carriers in Dirac materials can be the cause of their radiation resistivity.

I. Introduction : continued

I.3. Chirality and pseudospin of graphene: Experimental and theory

Tight binding approximation [P.R. Wallace (1947)]

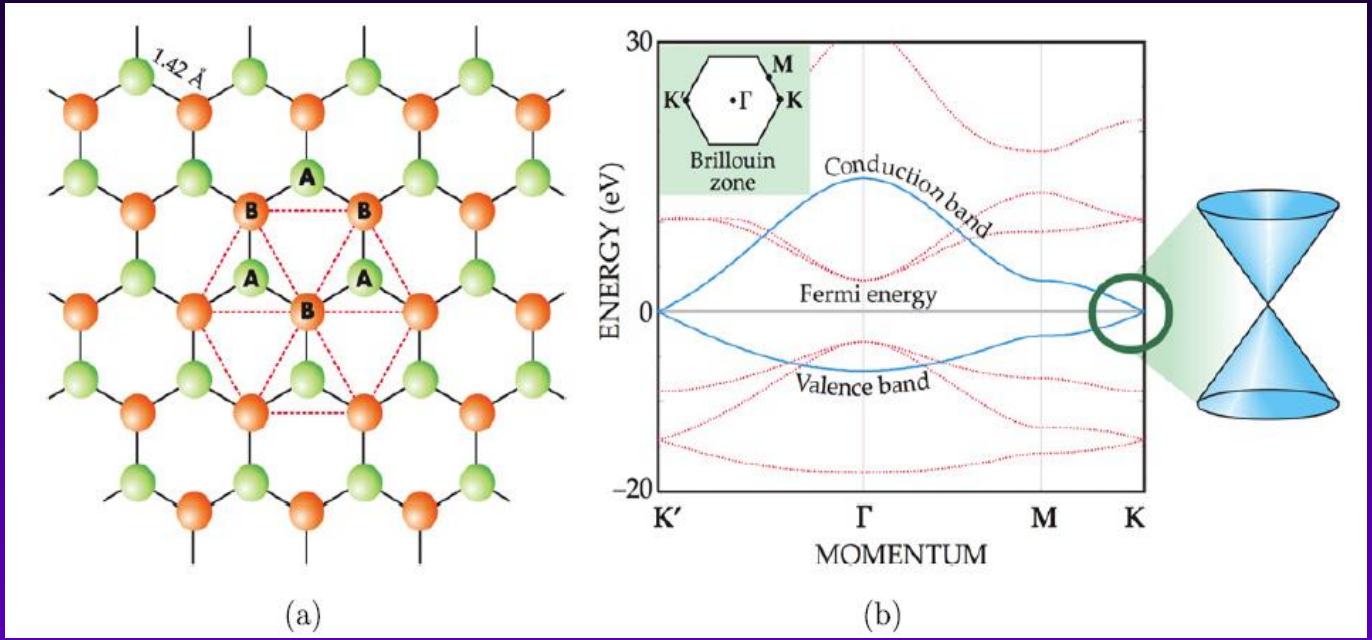

CHIRALITY AND PSEUDOSPIN OF GRAPHENE: EXPERIMENTAL AND THEORY

Linear energy dispersion and linear momentum cyclotron-mass dependence with zero cyclotron mass in Dirac point is evidence of mass absence for quasiparicles in graphene-like materials.

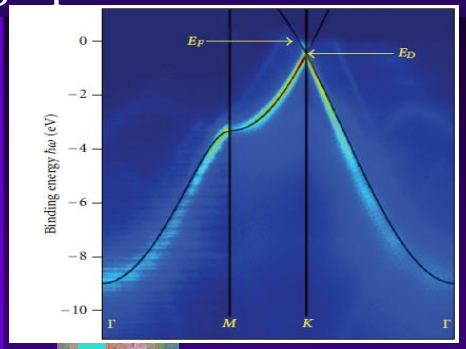

Figure : ARPES spectrum and band structure of graphene on top of SiC

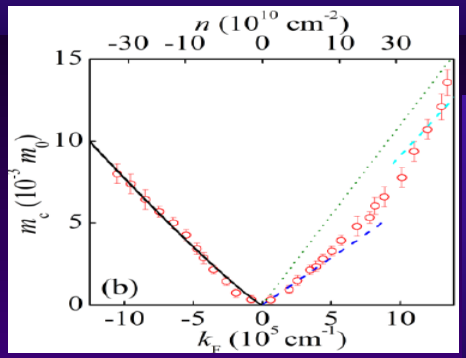

Figure : The effective cyclotron mass m_c from the Shubnikov – de Haas oscillations (SdHOs, cyclotron resonance)

Anomalous half-integer quantum Hall effect (QHE) happens owing the chirality-conservation law for massless charge carriers in graphene:

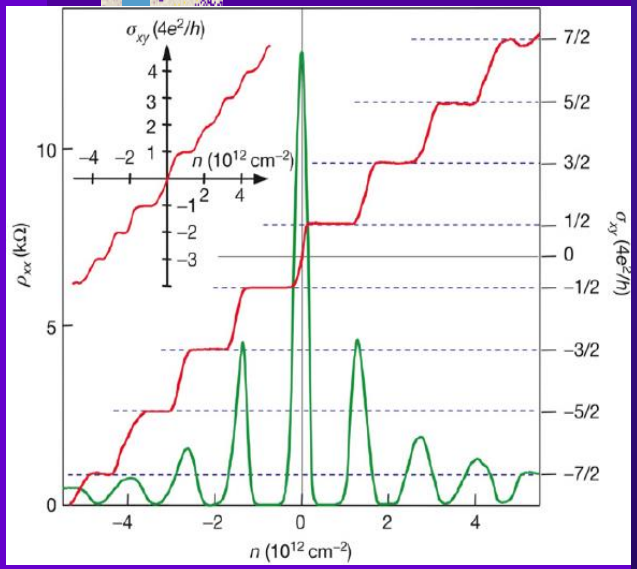

Figure : Hall conductivity σ_{xy} and corresponding longitudinal resistivity ρ_{xx} of graphene as a function of the charge-carrier density n measured at B = 14 T and T = 4K. The anomalous half-integer property of QHE is explained by the halved degeneracy of the zero-energy Landau level . The insert shows the Hall conductivity for bilayer graphene, which, in comparison, exhibits an integer QHE.

A quantized Landau level at zero energy is utilized by both electron and holes, which means that for Dirac-Fermions this level has half the degeneracy of the other levels, hence, this can be related to the two-fold degeneracy of the pseudospin.

II. Band structure of graphene and graphene-like materials

II.1. Chirality and Dirac massless fermions. Following equations of motion for quasi-particle excitations in different Dirac materials were proposed.

A low-energy $\boldsymbol{k}\cdot\boldsymbol{p}$-Hamiltonian for massless Dirac fermion reads

$$H_D = v_F \vec{\sigma}\cdot\vec{p}$$

This Hamiltonian is obtained using a Schrödinger equation in tight-binding approximation.

II.2. Topologically non-trivial charge carriers: Weyl nodes, Majorana zero-energy modes, chiral Majorana massless fermions

Weyl nodes appear after removing of Dirac point degeneration and lead to appearing Fermi arcs.

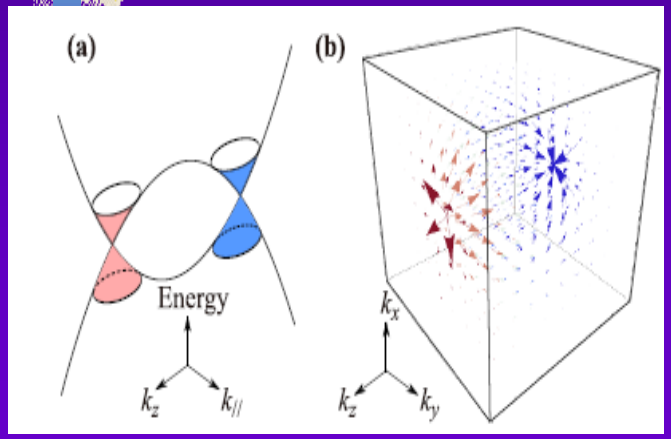

Figure : The conduction and valence bands of a topological semimetal touch at the **Weyl nodes** [H.-Zh. Lu, Sh.-Q. Shen (2017)]

II.2. Majorana zero energy mode, chiral Majorana massless fermions : continued

A high-energy $\boldsymbol{k}\cdot\boldsymbol{p}$-Hamiltonian for graphene-like materials is obtained within Dirac-Hartree-Fock self-consistent field and tight-binding approximations.

This motion equation describes a Majorana-like particle in a form of a superposition electrons and holes.

An equation of motion for a Majorana bispinor $(\psi^{\dagger}_{AB},(\psi^{*}_{BA})^{\dagger})$ in the monoatomic hexagonal layer (monolayer), comprised of two trigonal sublattices A, B reads [H.V.Grushevskaya, G.G. Krylov. Int. J. Nonlin. Comp. Sys. (2015); Symmetry (2016)]:

$$\left[\vec{\sigma}^{BA}_{2D}\cdot\vec{p}_{AB}-c^{-1}\widetilde{\Sigma_{AB}\Sigma_{BA}}\right]|\psi_{AB}\rangle=i\frac{\partial}{\partial t}|\psi^{*}_{BA}\rangle\,, \tag{1}$$

$$\left[\vec{\sigma}^{AB}_{2D}\cdot\vec{p}^{\,*}_{BA}-c^{-1}\left(\widetilde{\Sigma_{BA}\Sigma_{AB}}\right)^{*}\right]|\psi^{*}_{BA}\rangle=-i\frac{\partial}{\partial t}|\psi_{AB}\rangle\,. \tag{2}$$

Here, sublattice wave functions $|\psi_{AB}\rangle$ and $|\psi^{*}_{BA}\rangle$ relate to each other as follows:

$$|\psi^{*}_{BA}\rangle\propto\left(\Sigma^{x}_{rel}\right)_{BA}|\psi_{AB}\rangle\,, \tag{3}$$

$$|\psi_{AB}\rangle\propto\left(\Sigma^{x}_{rel}\right)_{AB}|\psi^{*}_{BA}\rangle\,; \tag{4}$$

$(\Sigma^{x}_{rel})_{AB} \equiv \Sigma_{AB}$, $(\Sigma^{x}_{rel})_{BA} \equiv \Sigma_{BA}$ are exchange interaction operators for the trigonal sublattices A, B of hexagonal lattice; mass operator terms $\widetilde{\Sigma_{BA(AB)}\Sigma_{AB(BA)}}$ are defined as

$$\widetilde{\Sigma_{BA(AB)}\Sigma_{AB(BA)}} = (i\Sigma^{x}_{rel})_{BA(AB)}\,(i\Sigma^{x}_{rel})_{AB(BA)}\,; \tag{5}$$

a transformed 2D vector $\vec{\sigma}^{AB}_{2D}$ of the Pauli matrices and a transformed 2D momentum $\vec{p}_{BA(AB)}$ are introduced as

$$\vec{\sigma}^{BA(AB)}_{2D} = (\Sigma^{x}_{rel})_{BA(AB)}\,\vec{\sigma}\,(\Sigma^{x}_{rel})^{-1}_{BA(AB)}\,, \tag{6}$$

$$\vec{p}_{BA(AB)} = (\Sigma^{x}_{rel})_{BA(AB)}\,\vec{p}\,(\Sigma^{x}_{rel})^{-1}_{BA(AB)}\,; \tag{7}$$

$\vec{\sigma}$ is a 2D vector of the Pauli matrices: $\vec{\sigma} = \{\sigma_1,\ \sigma_2\}$; $\vec{p}$ is a 2D momentum operator, c is the speed of light. One can see, that when neglecting the operator (5), the system of Eqs. (1), (2) are equations of motion for a Majorana-like massless particle.

The system of Eqs. (1), (2) can be approximated by a Dirac equation in the following way. Let us rewrite, for example, (1) for the steady state

$$\left[\vec{\sigma}_{2D}^{BA}\cdot\vec{p}_{AB}-c^{-1}\widetilde{\Sigma_{AB}\Sigma_{BA}}\right]|\psi_{AB}\rangle=E_{qu}\,|\psi_{BA}^{*}\rangle\,. \tag{8}$$

According to (6) and (7), the bispinor component $|\psi_{AB}\rangle$ can be obtained as $|\psi_{AB}\rangle=\Sigma_{AB}\left|\tilde{\psi}_{A}\right\rangle$. Due to (3) $\left|\tilde{\psi}_{A}\right\rangle$ defines also the component of the Majorana spinor $|\psi_{BA}^{*}\rangle$ as $|\psi_{BA}^{*}\rangle\propto\left(\Sigma_{rel}^{x}\right)_{BA}\left|\tilde{\psi}_{A}\right\rangle$. Hence

$$\Sigma_{BA(AB)}^{2}\propto\Sigma_{BA(AB)}. \tag{9}$$

II.2. Majorana zero energy mode, chiral Majorana massless fermions : continued

The following is used to simplify a solution of eigenvalue problem:

1) the quantum exchange matrix determines the operator of Fermi velocity entering in the high-energy graphene Hamiltonian as

$$\hat{v}_F = \Sigma_{BA}$$

2) the condition holds

$$\widehat{\psi}^*_{BA} = \alpha \Sigma_{BA} \widehat{\psi}^*_{BA} \Sigma^{-1}_{BA}$$

Then an approximate expression takes place in a form

$$|\psi_{AB}\rangle \approx \frac{\Sigma_{AB}\Sigma_{BA}}{\langle 0|\,\hat{v}_F\,|0\rangle}\,|\psi_{AB}\rangle = \frac{\left\{\alpha^{-1}\Sigma_{BA} + [\Sigma_{AB}, \Sigma_{BA}]\right\}}{\langle 0|\,\hat{v}_F\,|0\rangle}\,|\psi_{AB}\rangle = \left\{1 + \frac{(\Delta\Sigma + [\Sigma_{AB}, \Sigma_{BA}])}{\langle 0|\,\hat{v}_F\,|0\rangle}\right\}|\psi_{AB}\rangle$$

As result, one gets a Dirac-like equation

$$\left[\vec{\sigma}^{BA}_{2D} \cdot \vec{p}_{AB} - c^{-1}\widetilde{\Sigma_{AB}\Sigma_{BA}}\right]|\psi^*_{BA}\rangle = \tilde{E}\left\{1 + (\Delta\Sigma + [\Sigma_{AB}, \Sigma_{BA}])\,/\,\langle 0|\,\hat{v}_F\,|0\rangle\right\}|\psi^*_{BA}\rangle$$

We solved this equation.

II.2. Majorana zero energy mode, chiral Majorana massless fermions : continued

To prove existence of topologically non-trivial states it is necessary to calculate a Zak phase. **Zak phase** is determined as $\gamma(\vec{k}) = \oint_{C(\vec{k})} \langle u_m(\vec{k}) | \nabla_{\vec{k}} | u_m(\vec{k}) \rangle d\vec{k}$

A **Wilson loop operator** W is constructed as an exponent of $i\gamma$:

$$W = e^{-i\gamma} = \prod_{i=1}^{\infty} U_{i,i+1}$$

where elements $U_{i,i+1}^{m,n}$ of the matrix $U_{i,i+1}$ are scalar products of wave functions:

$U_{i,i+1}^{m,n} = \langle u_{n,\vec{k}} | u_{m,\vec{k}} \rangle$, m; n =1,…N enumerate bands; The Wilson loop serves the curve $C(\vec{k})$ being a side of equilateral triangle of variable size with a center of mass in the Dirac K(K')-point.

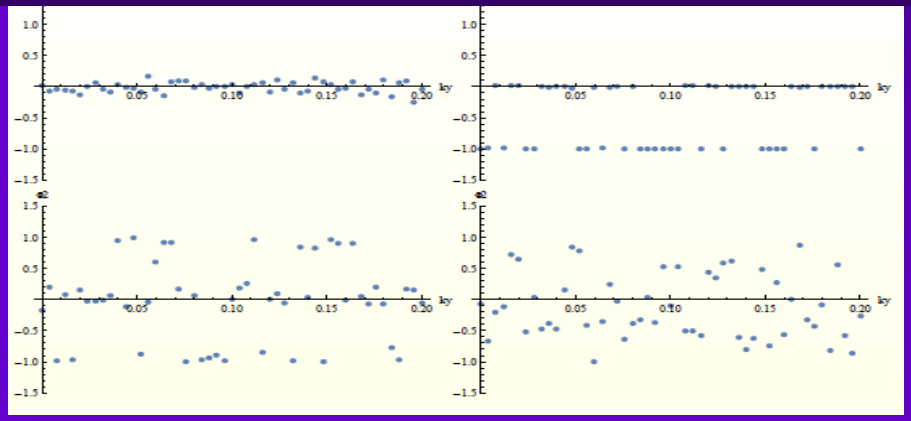

type of graphene model	Arg $W(k_x)$
Dirac massless fermion	$\{0, \pm\pi\}$
Majorana massless fermion	$\{0, \pm\pi/2, \pm\pi\}$

Figure : Numerical calculations of arguments of the Wilson-loop eigenvalues. Eigenvalues can be non-trivial ones and form a following cyclic group Z_2xZ_4 . It means that this graphene model is topologically non-trivial.

II.2. Majorana zero energy mode, chiral Majorana massless fermions : continued

Dichroism of Dirac bands

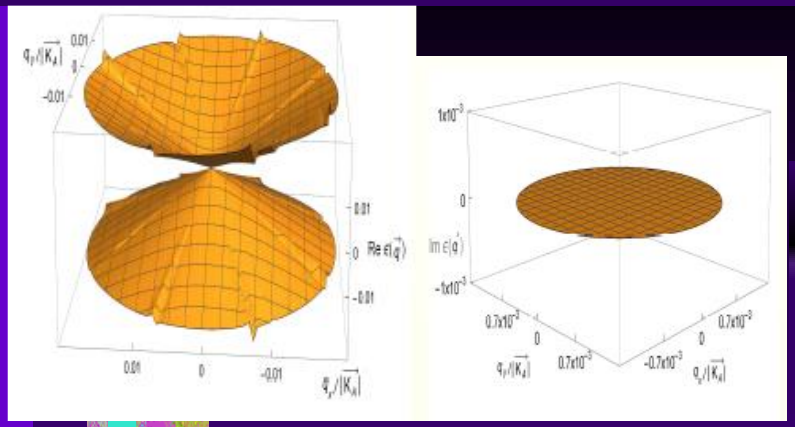

Figure: A band structure (real (on the left) and imaginary (on the right) parts) with the Majorana zero-energy modes in the Dirac cones apexes for semimetal model N = 3

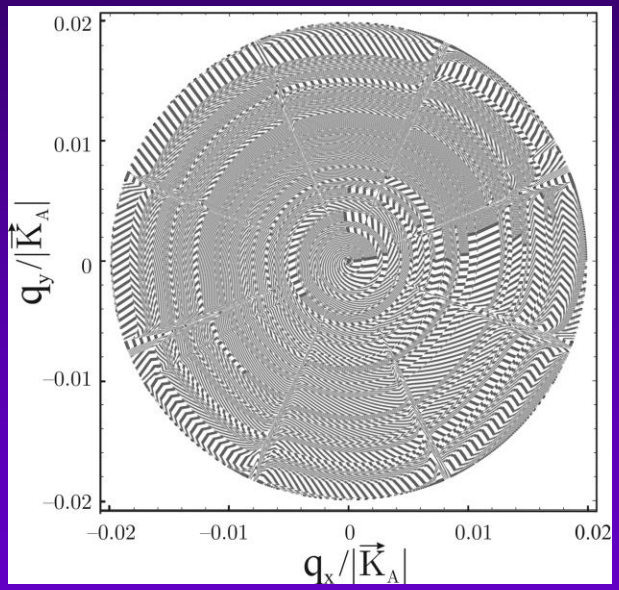

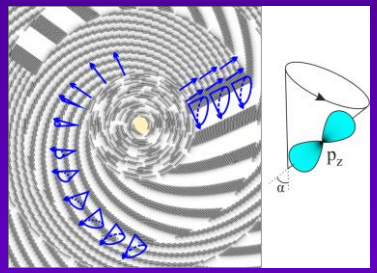

Figure: Band spin-orbit texture in contour plot (left) and a model vortex of precessing orbitals (right). The angle α is the precession angle of p_z-orbital

II.3. Chiral anomaly and deconfinement

Topological nontriviality of problem

Nonzero Zak phase means existence of topologically non-trivial states.

A Dirac particle is a superposition of two Majorana fermions. In this sense, the Majorana fermions is confined in Dirac particles. However, one of two eigenvalues of the dynamical-mass operator is equal to zero, accordingly, signature of majorana fermions is a chiral anomaly.

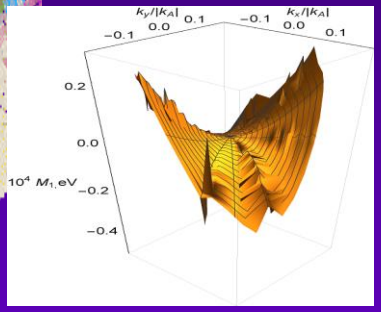

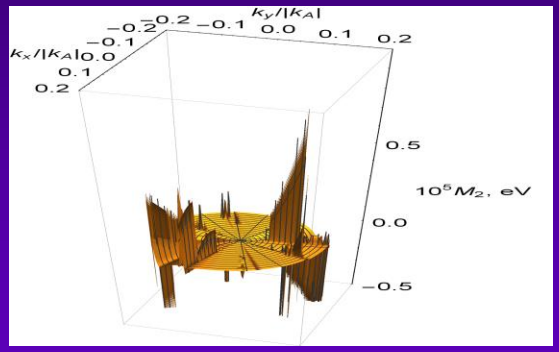

Figure: Eigenvalues of the mass operator (chiral anomaly)

III. Radiation resistivity of Langmuir-Blodgett (LB) thin films from carbon-nanotubes decorated by organometallic-compound

III.1. Spin-polarized surface states of thin LB-films from decorated MWCNTs

Samples have been fabricated by the Langmuir-Blodgett (LB) technique. LB-monolayers refers to graphen-like materials. Multiwalled carboxilated CNTs with diameter about 2.5 nm are used.

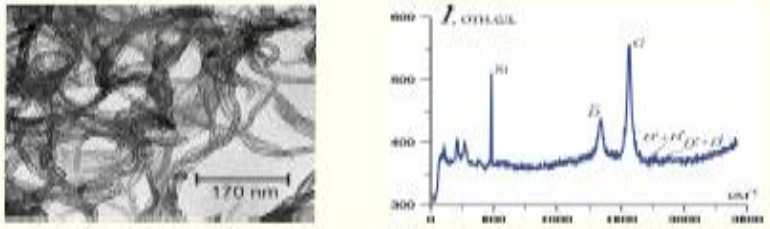

Figure: 3. (a) TEM-image of non-functionalized carboxylated multi-walled CNTs on formvar polymer coating;
(b) Raman spectrum of original carboxylated MWCNTs on Si

Graphene is a true two-dimensional semimetal. The use of CNT or graphene as sensitive elements is hampered due to the lack of free charge carriers at the Fermi level in graphene and graphene-like materials. Therefore they are decorated by metal atoms to activate spin-polarized currents (fig. 1).

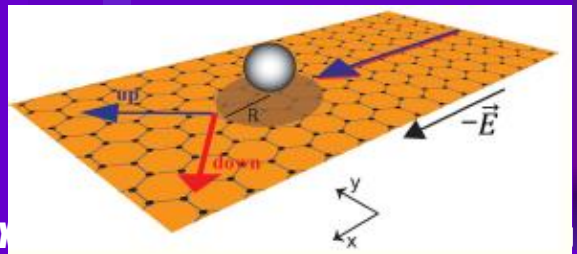

Spin-orbit splitting of the band dispersion occurs by bringing heavy metallic atoms in close contact to graphene. Under the action of Coulomb field of adatoms there appears a gap E_g in band structure of graphene and metallic graphene-like materials.

II.1. Spin-polarized surface states of thin LB-films from decorated MWCNTs: continued

But the decoration with small doses reduces and one with large doses suppresses the charge carrier mobility of graphene devices. Therefore, we decorated MWCNTs by complex of high-spin iron with dithionyl-pyrrolle ligands (see fig.).

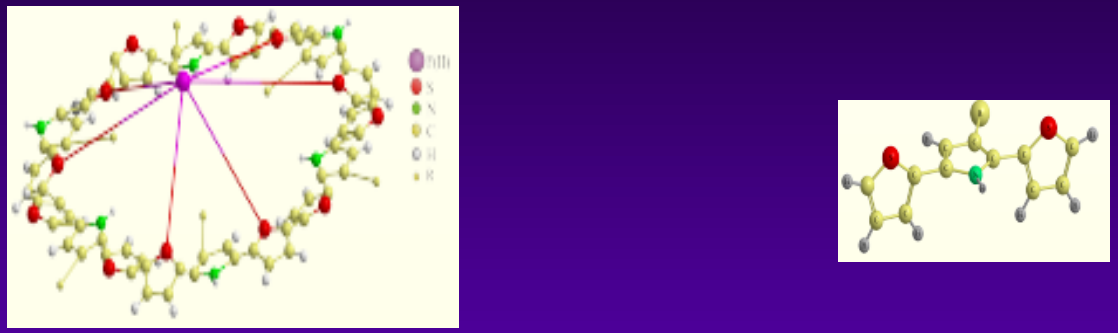

Figure: (left) Structure formula of a conducting oligomer 3-hexadecyl-2,5-di(thiophen-2-yl)-1H-pyrrole with chemically bounded hydrophobic 16-link hydrocarbon chain (DTP, thiophene-pyrrole) and (right) structure formula of complex of high-spin iron with dithionyl-pyrrolle ligands

II.1. Spin-polarized surface states of thin LB-films from decorated MWCNTs: continued

LB-film was deposited on planar capacitive sensor (see fig.) of interdigital-type on pyroceramics support to perform impedance measurements.

For electrochemical studies, we use a planar capacitive sensor of interdigital-type on pyroceramics support. Aluminum electrodes of the sensor are arranged in an Archimedes-type spiral configuration. A dielectric coating of the electrodes represents itself nanoporous anodic alumina layer (AOA) with a pore diameter of 10 nm.

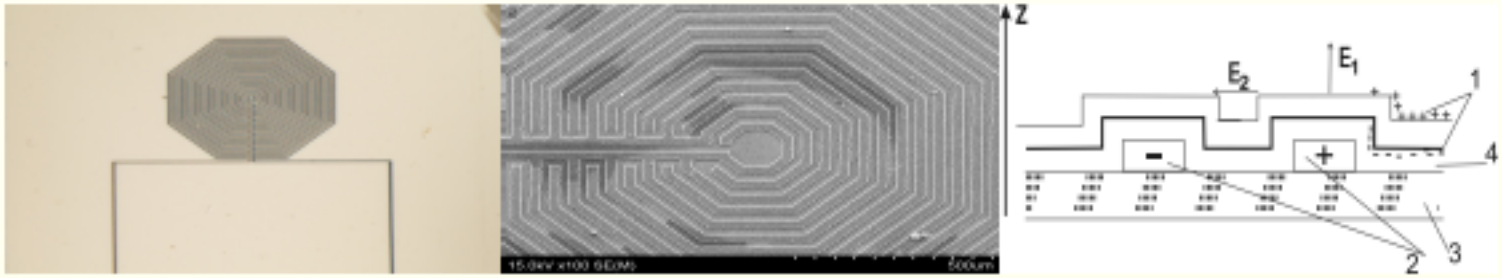

Figure: 7. (a, b) SEM images of sensor. (c) The model of i -th "open type" capacitor with thin film of nanoporous anodic alumina (AOA): 1 - double electrically charged layer that forms on the interface and includes nanopores filled by water, 2 -positive and negative electrodes, 3 - dielectric substrate of sensor, 4 - dielectric barrier layer of AOA; $\vec{E}_1$, $\vec{E}_2$ are electric field strengths near the electrodes.

II.1. Spin-polarized surface states of thin LB-films from decorated MWCNTs: continued

As you can see in this fig., a value of capacity of the sensor without LB-film is larger than for the sensor with LB-film. It happens because the conducting LB-film screens the electrode system.

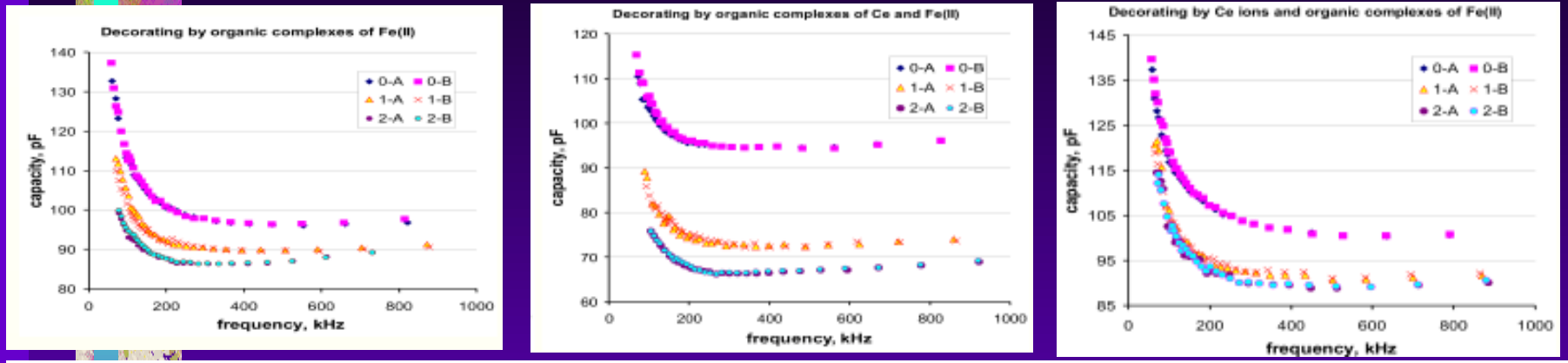

Figure: Cyclic frequency dependencies of capacity: (left) decorating by complex Fe(II), (middle) decorating by complex Ce and Fe(II), (right) decorating by Ce iones and complex Fe(II); for sensors without (0) and with dithionyl-pyrrolle LB-film (1) and MWCNTs (2) in deionized water. A and B denote direct and reverse branches, respectively.

III. Radiation resistivity of Langmuir-Blodgett (LB) thin films from carbon-nanotubes decorated by organometallic-compound : continued

III.2. Electrophysical response to ionizing low-energy gamma irradiation

The electrophysical properties of irradiated Langmuir-Blodgett (LB) thin films fabricated from MWCNTs decorated by the organometallic compound are studied. The irradiation conditions were chosen to be low-energy ones, but the low radiation fluxes can ionize film atoms. To produce the weak gamma-ray fluxes, we utilize cesium source ^{137}Cs emitting the gamma-quanta with energy E_γ = 662 keV, irradiation dose is 10^{-9} Gy. You can see radiation damaging of FeDTP-film leads to an increase of the its capacity immediately after the irrradiation. In 2 weeks after radiation the screening ability of the film increases sharply. But, in 3 months after radiation the electrophysical properties of the film recover.

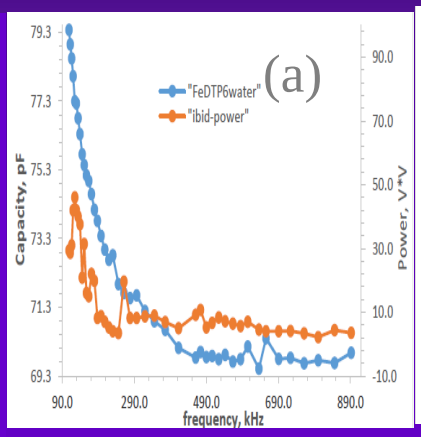

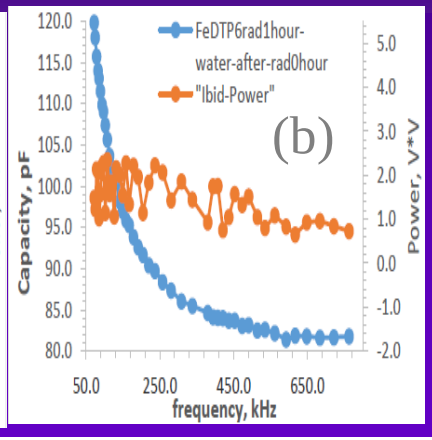

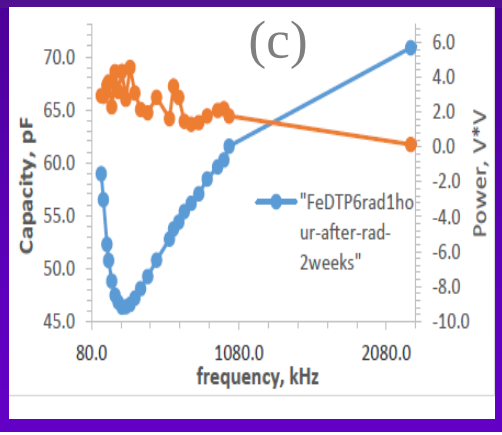

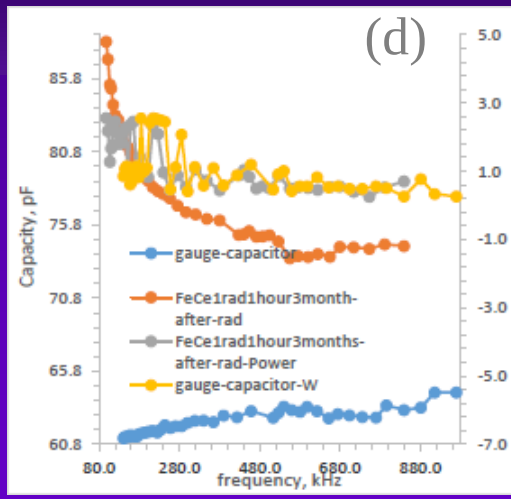

Figure: Frequency dependencies of capacity for organometallic Fe(II)DTP-film: (a) before irradiation; (b) immediately, (c) 2 weeks and (d) 3 months after the irradiation. Irradiation time is 1 hour.

III. Radiation resistivity of Langmuir-Blodgett (LB) thin films from carbon-nanotubes decorated by organometallic-compound : continued

III.2. Electrophysical response to ionizing low-energy gamma irradiation: continued

The electrophysical properties of irradiated Langmuir-Blodgett (LB) thin films fabricated from MWCNTs decorated by an organometallic complexes are represented. You can see the radiation damaging of MWCNT-film is absent already at once, because an decreasing capacity holds immediately after the irrradiation. In 3 weeks after radiation the screening ability of the film increases still more. In 3 and 5 months after radiation the high values of screening of the film remains.

So, the value of complex dielectric permittivity increases for the irradiation of organometallic thin LB-films without CNTs. Then, after some time, a restructuring proceeds that leads to a screening effect. Unlike, the irradiated MWCNT-containing LB-films immediately acquire high-screening properties.

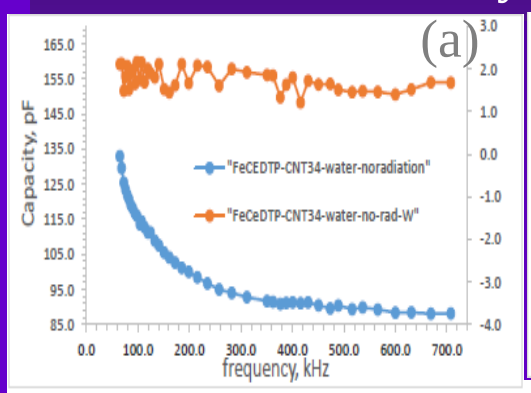

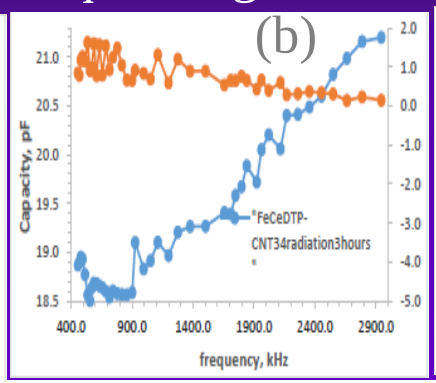

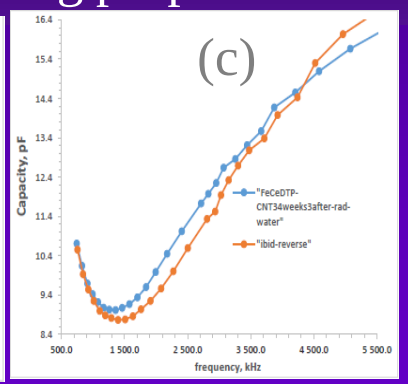

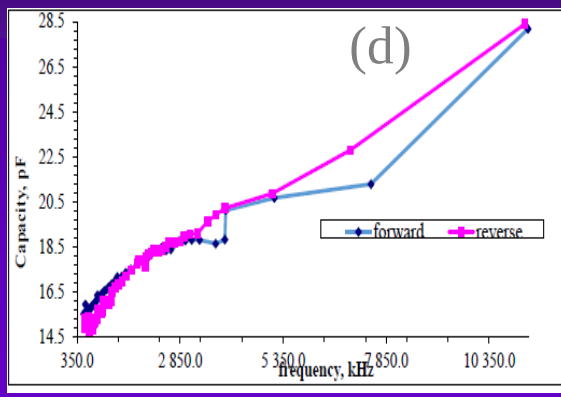

Figure: Frequency dependencies of capacity for MWCNT-film: (a) before irradiation; (b) immediately, (c) 3 weeks and (d) 3 months after the irradiation. Irradiation times are 1 and 3 hours.

III. Radiation resistivity of Langmuir-Blodgett (LB) thin films from carbon-nanotubes decorated by organometallic-compound : continued

III.3. Emergence of 2D chiral-Magorana-particle gas after irradiation

Let me discuss possible mechanisms for the emergence of such irradiation surface-defects.

III.3. 1. Many-body interactions.

Hartree – Fock theory predicts logarithmic divergence of Fermi velocity in the Dirac point due to electron-electron interactions. It should lead to puddles of localized electrons and holes. Indeed, for suspended graphene, electron-electron interactions increase the Fermi velocity v_F near the Dirac point on experimental data. However, meanwhile a bandgap is absent. Accordingly, subgap surface-defect states may not appear within the Hartee-Fock theory.

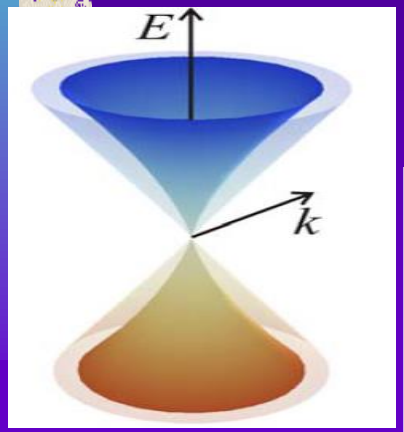

Figure: Sketch of graphene's electronic spectrum with and without taking into account e-e interactions. The outer cone is the single-particle spectrum $E = v_F \hbar k$, and the inner cone illustrates the many-body spectrum observed in experiments.

III.3. Emergence of 2D chiral-Magorana-particle gas after irradiation: continued

A Kitaev model atomic chain [Kitaev (2001)] is based on a Majorana quess that a Dirac fermion is two Majorana particles superposition.

The Majorana fermion [Qi Zhang, Biao Wu (2018)]

$$\gamma_{j,\theta} = c_j^{\dagger} e^{2i\theta} + c_j e^{-2i\theta}$$

is a superposition of two Dirac fermions c_j and c_j^{+}.

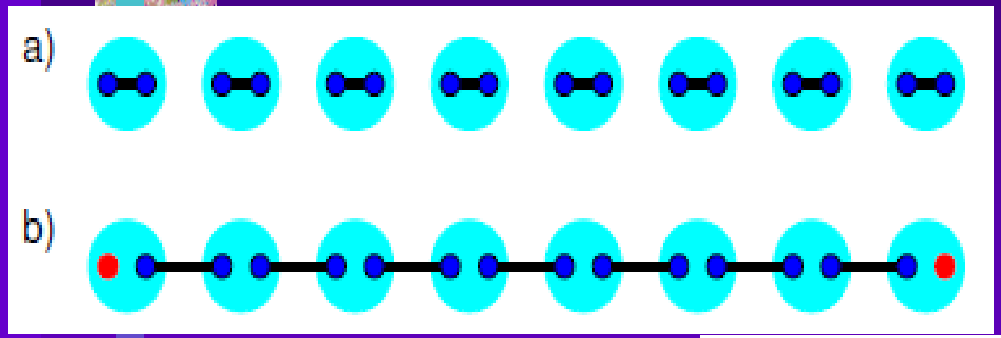

Figure: Two phases of the Kitaev chain. a) In the trivial phase Majorana fermions on each lattice site can be thought as bound into ordinary fermions.
b) In the topological phase Majoranas on neighboring sites are bound leaving two unpaired Majorana fermions at the ends of the chain.

III.3. Emergence of 2D chiral-Magorana-particle gas after irradiation: continued

III.3. 2. Kitaev model: continued

Majorana states are bound to the ends of atomic chain and are zero-energy modes within energy gap.

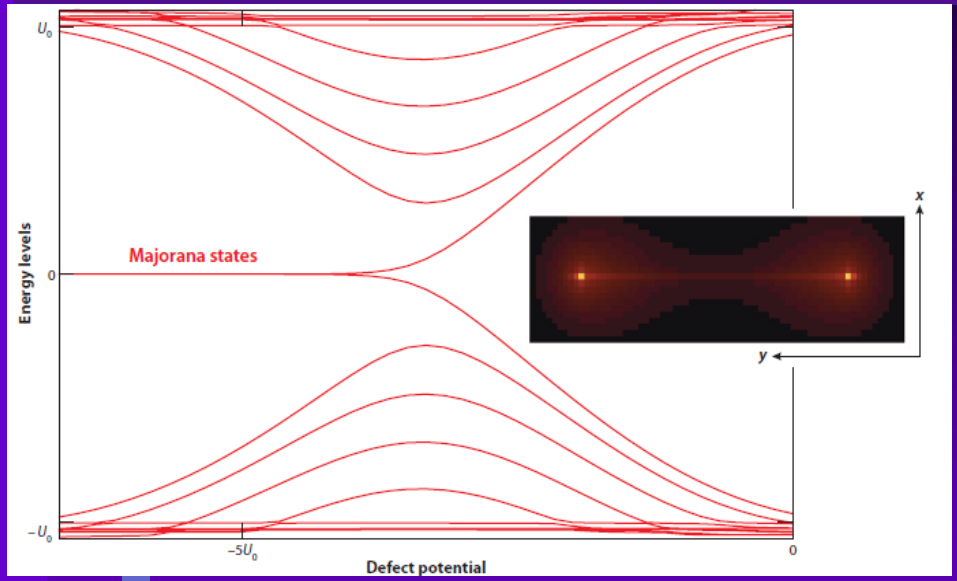

Figure: Emergence of a pair of zero-energy Majorana states in a model electrostatic line defect.

Majorana-like zero-energy particles are a core (sink or antisink) of vortex, and topology prevents their decay. Unfortunately, within the Kitaev model an excitation leads to loss of the topology. Therefore, it does not explain the emerging long-life-time surface defects under irradiation.

III.3. Emergence of 2D chiral-Magorana-particle gas after irradiation: continued

III.3. 3. Chiral Majorana massless fermions

One can consider CNT as chain from Majorana modes γ_i, i=1,…,N with zero energy in ground state. The Majorana particles are paired within the chain and unpaired at chain ends. Majorana subgap states are bound to the ends of atomic chain. Calculations performed in [Qi Zhang, Biao Wu (2018)] showed, that these states are independent.

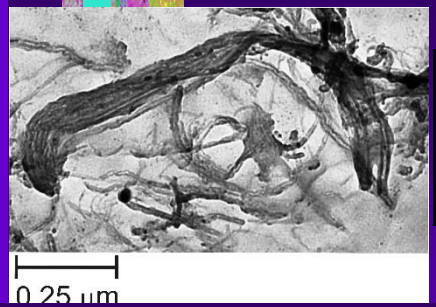

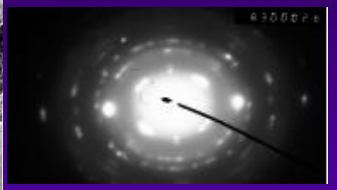

TEM-image of MWCNT-LB-cluster on support from the metal-contained thiophene-pyrrole LB-film

In LB-film the CNTs ends are anchored in the conducting FeDTP-monolayer. Meanwhile closed conducting contours are created. Therefore, effectively, the surface CNT states represent themselves 2D Majorana gas of zero-energy modes in ground state.

As you see in the high-energy graphene model with chiral Majorana massless fermions the Dirac point (Majorana zero-energy mode) hosts a vortex.

III. Radiation resistivity of Langmuir-Blodgett (LB) thin films from carbon-nanotubes decorated by organometallic-compound : continued

III.3. Emergence of 2D chiral-Magorana-particle gas after irradiation: continued

III.3. 3. Chiral Majorana massless fermions : continued

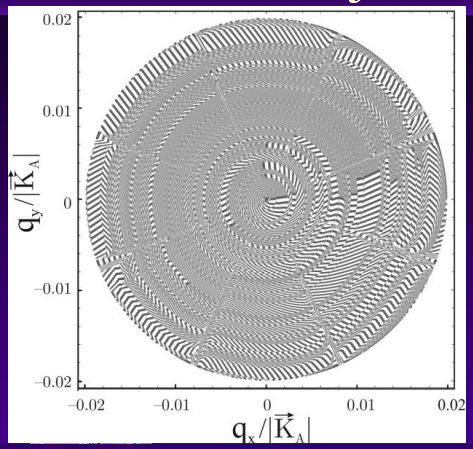

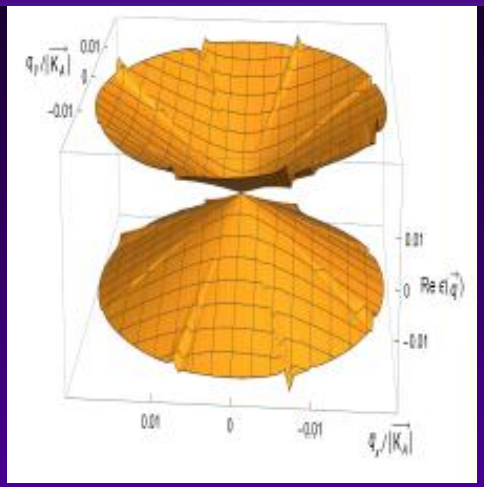

The core acquires vortex “cavity” at exitation. Therefore, the subgap radiation-defect states are different vortices with cores which represent themselves more low-energy vortices.

Symmetry of these subgap states and states emerging in the subreplica region is different. Therefore the radiation surface-defects are symmetry protected ones.

III.3. Emergence of 2D chiral-Magorana-particle gas after irradiation: continued

III.3. 3. Chiral Majorana massless fermions : continued

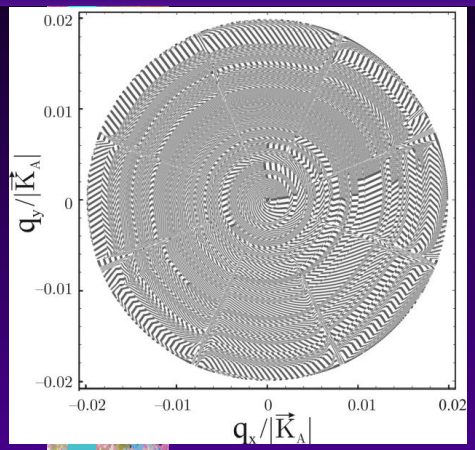

Vortices emerge in pairs and their density ρ is infinite large:

$$\rho \to \infty.$$

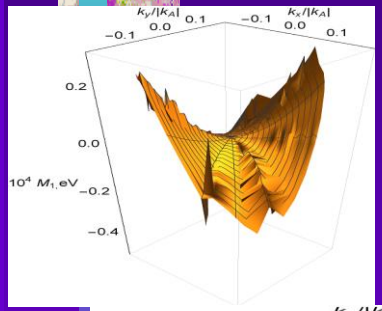

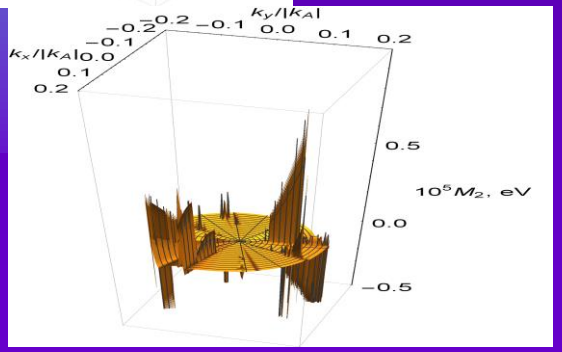

One vortex in the Majorana spin-polarized pair holds zero mass and remains its chirality. The other vortex acquires nonzero mass. As result, there is single Majorana-like particle, an energy of which can not dissipate in heat due to a law of helicity conservation. A statistics of vortex system is **non-abelian** one. Due to the **non-abelian statistics** of these carriers, these quasi-particle excitations can not decay.

III. Radiation resistivity of Langmuir-Blodgett (LB) thin films from carbon-nanotubes decorated by organometallic-compound : continued

III.3. Emergence of 2D chiral-Magorana-particle gas after irradiation: continued

III.3. 3. Chiral Majorana massless fermions : continued

Since MWCNTs are decorated by octahedral complexes of high-spin Fe(II), all Majorana states of the CNT-monolayer are spin-polarized ones. Accordingly, very big number of sustained free charge carriers appear. Owing to this one observes the sharp increase of screening degree for the irradiation CNT-monolayer.

III. Radiation resistivity of Langmuir-Blodgett (LB) thin films from carbon-nanotubes decorated by organometallic-compound : continued

III.3. Emergence of 2D chiral-Magorana-particle gas after irradiation: continued

III.3. 3. Chiral Majorana massless fermions : continued

Figure : TEM-image (left) and scheme (right) of LB-film from Fe-DTP complexes

The metal-containing LB-DTP-film represents itself a network of Kitaev's linked chains with Majorana quasi-particles at ends also. However, in the LB-DTP-monolayer a 2D gas of zero-energy modes consists of two subsystems spin-polarized oppositely. There exist both left- and right-handed Majorana-like vortex particles. Since very big number of free charge-carriers appear one observes a sharp increase of screening degree for the DTP-monolayer.

Then these left- and right-handed Majorana particles form chiral massless Dirac quasi-particles (electrons and holes) that recovers the previous electro-physical properties after a relaxation process.

Conclusion

Perspectives and applications:

1) Preventing from cosmic rays and space radiation, radiation-resistent nanoelectronics, detectors
2) Robust quantum computation with braiding Majoranas, realization of Majorana device

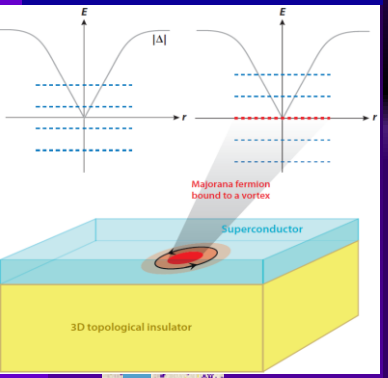

Figure: Profile of the superconducting pair potential Δ(r) in an Abrikosov vortex (solid gray curves) and bound electron-hole states in the vortex core (dashed dark blue lines). The left graph shows the usual sequence of levels in an s-wave superconductor, arranged symmetrically around zero energy. The right graph shows the level sequence when superconductivity is induced on the surface of a 3D topological insulator, with a nondegenerate state at E= 0. This midgap state is a Majorana fermion. Disadvantages are absence of Majorana braiding and relatively small life-time for such fermions.

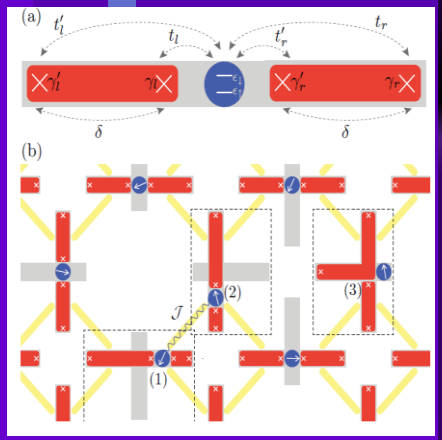

a) Setup of two 1D TSCs (InAs) (red bars) furnishing two MFs (γ's) on the left TSC, and two MFs on the right TSCin contact with a nontopological SC (gray); the MFs o each TSC can overlap, causing a splitting δ. Between the two TSCs is a quantum dot (blue disk) with two single-electron levels of up, ↑, and down, ↓, spin. The MFs are coupled to the dot through the tunneling elements tv and $t'v$, where v labels the right (r) and left (l) TSCs.

b) A network of TSCs where a grid of hybrid qubits (red and gray crosses) are long-distance coupled by tunably connecting the spin-1/2 quantum dots, with strength J, via floating gates (solid yellow lines), e.g., hybrid qubit (1) is coupled to hybrid qubi (2).

Thank you for your attention !